

# Ray-tracing through the Millennium Simulation: Born corrections and lens-lens coupling in cosmic shear and galaxy-galaxy lensing

S. Hilbert<sup>1\*</sup>, J. Hartlap<sup>2</sup>, S.D.M. White<sup>1</sup>, and P. Schneider<sup>2</sup>

<sup>1</sup> Max Planck Institute for Astrophysics, Karl-Schwarzschild-Str. 1, D-85741 Garching, Germany

<sup>2</sup> Argelander-Institut für Astronomie, Universität Bonn, Auf dem Hügel 71, D-53121 Bonn, Germany

Received / Accepted

## ABSTRACT

**Context.** Weak-lensing surveys need accurate theoretical predictions for interpretation of their results and cosmological-parameter estimation.

**Aims.** We study the accuracy of various approximations to cosmic shear and weak galaxy-galaxy lensing and investigate effects of Born corrections and lens-lens coupling.

**Methods.** We use ray-tracing through the Millennium Simulation, a large  $N$ -body simulation of cosmic structure formation, to calculate various cosmic-shear and galaxy-galaxy-lensing statistics. We compare the results from ray-tracing to semi-analytic predictions.

**Results.** (i) We confirm that the linear approximation (i.e. neglecting lensing effects beyond first order in density fluctuations) provides an excellent fit to cosmic-shear power spectra as long as the actual matter power spectrum is used as input. Common fitting formulae, however, strongly underestimate the cosmic-shear power spectra (by  $> 30\%$  on scales  $\ell > 10000$ ). Halo models provide a better fit to cosmic shear-power spectra, but there are still noticeable deviations ( $\sim 10\%$ ). (ii) Cosmic-shear B-modes, which are induced by Born corrections and lens-lens coupling, are at least three orders of magnitude smaller than cosmic-shear E-modes. Semi-analytic extensions to the linear approximation predict the right order of magnitude for the B-mode. Compared to the ray-tracing results, however, the semi-analytic predictions may differ by a factor two on small scales and also show a different scale dependence. (iii) The linear approximation may under- or overestimate the galaxy-galaxy-lensing shear signal by several percent due to the neglect of magnification bias, which may lead to a correlation between the shear and the observed number density of lenses.

**Conclusions.** (i) Current semi-analytic models need to be improved in order to match the degree of statistical accuracy expected for future weak-lensing surveys. (ii) Shear B-modes induced by corrections to the linear approximation are not important for future cosmic-shear surveys. (iii) Magnification bias can be important for galaxy-galaxy-lensing surveys.

**Key words.** gravitational lensing – dark matter – large-scale structure of the Universe – cosmology: theory – methods: numerical

## 1. Introduction

During the past few years, weak gravitational lensing has developed rapidly from mere detection to an important cosmological tool (Munshi et al. 2008). Measurements of cosmic shear help us to constrain the properties of the cosmic matter distribution (e.g. Semboloni et al. 2006; Hoekstra et al. 2006; Simon et al. 2007; Benjamin et al. 2007; Massey et al. 2007b; Fu et al. 2008), the growth of structure (e.g. Bacon et al. 2005; Massey et al. 2007c), and the nature of the dark energy (e.g. Taylor et al. 2007; Schimd et al. 2007; Amendola et al. 2008). Weak galaxy-galaxy lensing can be used to study the properties of galactic dark-matter halos and the relation between luminous and dark matter (e.g. Mandelbaum et al. 2006; Simon et al. 2007; Gavazzi et al. 2007).

The accuracy that can be reached in weak-lensing surveys is determined by several factors. On the observational side, high accuracy requires large field sizes and deep observations with a high number density of galaxies with mea-

surable shapes. Moreover, it is crucial to obtain an accurate and unbiased measurement of galaxy ellipticities. Finally, for the interpretation of the resulting data and the inference of cosmological parameters, an accurate theoretical model is needed. A thorough understanding of systematic effects in weak lensing will become particularly important with the advent of very large weak-lensing surveys such as CFHTLS<sup>1</sup>, KIDS<sup>2</sup>, Pan-STARRS<sup>3</sup>, and LSST<sup>4</sup>, or the planned Dark Energy Survey<sup>5</sup>, DUNE (Réfrégier et al. 2006), and SNAP<sup>6</sup>. For these surveys, the statistical uncertainties will be very small, so the accuracy will be limited by the remaining systematics in the data reduction and theoretical modeling.

While significant improvement on image-ellipticity measurements are expected in the near future (Massey et al.

<sup>1</sup> <http://www.cfht.hawaii.edu/Science/CFHLS>

<sup>2</sup> <http://http://www.astro-wise.org/projects/KIDS>

<sup>3</sup> <http://pan-starrs.ifa.hawaii.edu>

<sup>4</sup> <http://www.lsst.org>

<sup>5</sup> <http://www.darkenergysurvey.org>

<sup>6</sup> <http://snap.lbl.gov>

\* [hilbert@mpa-garching.mpg.de](mailto:hilbert@mpa-garching.mpg.de)

2007a), one still needs to investigate, how uncertain current theoretical predictions are, and how much improvement can be expected. Presently, the most accurate way to obtain predictions for weak-lensing surveys is to perform ray-tracing through large high-resolution  $N$ -body simulations of cosmic structure formation (Wambsganss et al. 1998; Jain et al. 2000; Hamana & Mellier 2001; Vale & White 2003). The drawback of this approach is that large  $N$ -body simulations are computationally demanding, so using them to explore the whole parameter space of cosmological models is currently unrealistic. On the other hand, ray-tracing simulations enable one to check the approximations and assumptions made in computationally less demanding (semi-)analytic models, and adjust and extend these models where necessary.

In this work, we employ ray-tracing through the Millennium Simulation (Springel et al. 2005) to study weak lensing. One of the largest  $N$ -body simulations available today, the Millennium Simulation provides not only a much larger volume, but also a higher spatial and mass resolution than simulations used for earlier weak-lensing studies. In order to take full advantage of the large simulation volume and high resolution, the ray-tracing algorithm used here differs in several aspects from algorithms used in previous works (e.g. Jain et al. 2000). Here, we give a detailed description of our ray-tracing algorithm.

Weak-lensing predictions are usually based on the linear approximation, in which light deflections are only considered to first order in the peculiar gravitational potential and hence, to first order in the matter fluctuations. The ray-tracing approach allows us to look at effects neglected in the linear approximation such Born corrections and lens-lens coupling. Here, we investigate the cosmic-shear B-modes induced by these effects and compare the ray-tracing results to semi-analytic estimates (Cooray & Hu 2002; Shapiro & Cooray 2006), whose accuracy has not been confirmed by numerical simulations yet. Moreover, we investigate how well fitting formulae (Peacock & Dodds 1996; Eisenstein & Hu 1999; Smith et al. 2003) and halo models (Seljak 2000; Cooray & Sheth 2002) reproduce cosmic-shear power spectra. Finally, we investigate the accuracy of the linear approximation for weak galaxy-galaxy lensing.

The paper is organized as follows. In the next section, we introduce the theoretical background and notation used in our lensing analysis. In Sec. 3, we discuss our ray-tracing algorithm. The results from our ray-tracing analysis are presented in Sec. 4. We conclude our paper with a summary in Sec. 5.

## 2. Theory

### 2.1. Gravitational light deflection

In this section, we introduce the formulae relating the ‘apparent’ positions of distant light sources to their ‘true’ positions. In order to label spacetime points in a model universe with a weakly perturbed Friedmann-Lemaître-Robertson-Walker (FLRW) metric, we choose a coordinate system  $(t, \boldsymbol{\beta}, w)$  based on physical time  $t$ , two angular coordinates  $\boldsymbol{\beta} = (\beta_1, \beta_2)$ , and the line-of-sight comoving distance  $w$  relative to the observer. The spacetime metric of the model universe is then given by (see, e.g., Bartelmann & Schneider

2001):

$$ds^2 = \left(1 + \frac{2\Phi}{c^2}\right) c^2 dt^2 - \left(1 - \frac{2\Phi}{c^2}\right) a^2 \times \left\{ dw^2 + f_K^2(w) [d\beta_1^2 + \cos^2(\beta_1) d\beta_2^2] \right\}. \quad (1)$$

Here,  $c$  denotes the speed of light,  $a = a(t)$  denotes the scale factor, and  $\Phi = \Phi(t, \boldsymbol{\beta}, w)$  denotes the peculiar (Newtonian) gravitational potential. The comoving angular diameter distance is defined as:

$$f_K(w) = \begin{cases} 1/\sqrt{K} \sin(\sqrt{K}w) & \text{for } K > 0, \\ w & \text{for } K = 0, \text{ and} \\ 1/\sqrt{-K} \sinh(\sqrt{-K}w) & \text{for } K < 0, \end{cases} \quad (2)$$

where  $K$  denotes the curvature of space. The particular choice for the angular coordinates  $\boldsymbol{\beta} = (\beta_1, \beta_2)$  is convenient for the application of the ‘flat-sky’ approximation, where the metric near  $\boldsymbol{\beta} = \mathbf{0}$  is approximated using  $\cos^2(\beta_1) \approx 1$ .

Consider the path, parameterized by comoving distance  $w$ , of a photon eventually reaching the observer from angular direction  $\boldsymbol{\theta}$ . The angular position  $\boldsymbol{\beta}(\boldsymbol{\theta}, w)$  of the photon at comoving distance  $w$  is then given by (see, e.g., Jain & Seljak 1997, for a sketch of a derivation):

$$\boldsymbol{\beta}(\boldsymbol{\theta}, w) = \boldsymbol{\theta} - \frac{2}{c^2} \int_0^w dw' \frac{f_K(w-w')}{f_K(w)f_K(w')} \times \nabla_{\boldsymbol{\beta}} \Phi(t(w'), \boldsymbol{\beta}(\boldsymbol{\theta}, w'), w') \quad (3)$$

with  $\nabla_{\boldsymbol{\beta}} = (\partial/\partial\beta_1, \partial/\partial\beta_2)$ , and  $t(w')$  denoting the cosmic time of events at line-of-sight comoving distance  $w'$  from the observer. By differentiation this equation w.r.t.  $\boldsymbol{\theta}$ , we obtain the distortion matrix  $\mathbf{A}$ , i.e. the Jacobian of the lens mapping  $\boldsymbol{\theta} \mapsto \boldsymbol{\beta} = \boldsymbol{\beta}(\boldsymbol{\theta}, w)$ :

$$\begin{aligned} A_{ij}(\boldsymbol{\theta}, w) &= \frac{\partial\beta_i(\boldsymbol{\theta}, w)}{\partial\theta_j} \\ &= \delta_{ij} - \frac{2}{c^2} \int_0^w dw' \frac{f_K(w-w')}{f_K(w)f_K(w')} \\ &\quad \times \frac{\partial^2\Phi(t(w'), \boldsymbol{\beta}(\boldsymbol{\theta}, w'), w')}{\partial\beta_i\partial\beta_k} A_{kj}(\boldsymbol{\theta}, w'). \end{aligned} \quad (4)$$

Due to the matrix products in (4), the distortion matrix  $\mathbf{A}$  is generally not symmetric. However, it can be decomposed into a rotation matrix (related to a usually unobservable rotation in the source plane) and a symmetric matrix (Schneider et al. 1992):

$$\mathbf{A}(\boldsymbol{\theta}, w) = \begin{pmatrix} \cos\varphi & \sin\varphi \\ -\sin\varphi & \cos\varphi \end{pmatrix} \times \begin{pmatrix} 1 - \kappa - \gamma_1 & -\gamma_2 \\ -\gamma_2 & 1 - \kappa + \gamma_1 \end{pmatrix}. \quad (5)$$

The decomposition defines the rotation angle  $\varphi = \varphi(\boldsymbol{\theta}, w)$ , the convergence  $\kappa = \kappa(\boldsymbol{\theta}, w)$ , and the two components  $\gamma_1 = \gamma_1(\boldsymbol{\theta}, w)$  and  $\gamma_2 = \gamma_2(\boldsymbol{\theta}, w)$  of the shear, which may be combined into the complex shear  $\gamma = \gamma_1 + i\gamma_2$ .

The shear field  $\gamma(\boldsymbol{\theta}, w)$  can be decomposed into a rotation-free part  $\gamma_E(\boldsymbol{\theta}, w)$  and a divergence-free part

$\gamma_{\text{B}}(\boldsymbol{\theta}, w)$ . For infinite fields, the decomposition into these *E/B-modes* is most easily written down in Fourier space:

$$\hat{\gamma}_{\text{E}}(\boldsymbol{\ell}, w) = \frac{\ell^2}{|\ell|^4} [(\ell_1^2 - \ell_2^2)\hat{\gamma}_1(\boldsymbol{\ell}, w) + 2\ell_1\ell_2\hat{\gamma}_2(\boldsymbol{\ell}, w)], \quad (6a)$$

$$\hat{\gamma}_{\text{B}}(\boldsymbol{\ell}, w) = \frac{\ell^2}{|\ell|^4} [(\ell_1^2 - \ell_2^2)\hat{\gamma}_2(\boldsymbol{\ell}, w) - 2\ell_1\ell_2\hat{\gamma}_1(\boldsymbol{\ell}, w)]. \quad (6b)$$

Here, hats denote Fourier transforms,  $\boldsymbol{\ell} = (\ell_1, \ell_2)$  denotes the Fourier wave vector, and  $\ell = \ell_1 + i\ell_2$ . Care must be taken when decomposing the shear in fields of finite size, where the field boundaries can cause artifacts (Seitz & Schneider 1996). These artifacts can be avoided by using aperture masses to quantify the shear E- and B-mode contributions (Crittenden et al. 2002; Schneider et al. 2002).

Equations (3) and (4) are implicit relations for the light path and the Jacobian. The solution of Eq. (3) to linear order in the potential is obtained by integrating along undisturbed light paths:

$$\boldsymbol{\beta}(\boldsymbol{\theta}, w) = \boldsymbol{\theta} - \frac{2}{c^2} \int_0^w dw' \frac{f_K(w-w')}{f_K(w)f_K(w')} \times \nabla_{\boldsymbol{\theta}} \Phi(t(w'), \boldsymbol{\theta}, w') \quad (7)$$

The distortion to linear order reads:

$$A_{ij}(\boldsymbol{\theta}, w) = \delta_{ij} - \frac{2}{c^2} \int_0^w dw' \frac{f_K(w-w')}{f_K(w)f_K(w')} \times \frac{\partial^2 \Phi(t(w'), \boldsymbol{\theta}, w')}{\partial \theta_i \partial \theta_k}. \quad (8)$$

The linear approximation to the distortion contains the *Born approximation*, which ignores deviations of the actual light path from the undisturbed path on the r.h.s. of Eq. (4). Moreover, *lens-lens coupling* is neglected, i.e. the appearance of the distortion on the r.h.s. of Eq. (4). The neglected lens-lens coupling and corrections to the Born approximation account for the effect that light from a distant source “sees” a distorted image of the lower-redshift matter distribution due to higher-redshift matter inhomogeneities along the line-of-sight. Thus, the linear approximation works well in regions where larger matter inhomogeneities are absent or confined to a small redshift range, but fails in regions where noticeable distortions arise from matter inhomogeneities at multiple redshifts.

Born corrections and lens-lens coupling effects may create shear B-modes. The calculation of the shear B-modes to lower order by iteratively solving (4) is possible (Cooray & Hu 2002), but tedious, and the accuracy of this perturbative approach is not known. However, multiple deflections and lens-lens coupling effects are fully included in the multiple-lens-plane approximation as described below. We will thus use this approximation to investigate these effects and assess the quality of perturbative calculations of these effects.

## 2.2. The multiple-lens-plane approximation

In the multiple-lens-plane approximation (see, e.g., Blandford & Narayan 1986; Schneider et al. 1992; Seitz et al. 1994; Jain et al. 2000), a series of lens planes perpendicular to the central line-of-sight is introduced into the observer’s backward light cone. The continuous deflection

that a light ray experiences while propagating through the matter inhomogeneities in the light cone is then approximated by finite deflections at the lens planes. The deflections are calculated from a projected matter distribution on the lens planes. This corresponds to solving the integral equations (3) and (4) by discretization (and using the impulse approximation).

The deflection  $\boldsymbol{\alpha}^{(k)}(\boldsymbol{\beta}^{(k)})$  of a light ray intersecting the  $k^{\text{th}}$  lens plane (here, we count from the observer to the source) at angular position  $\boldsymbol{\beta}^{(k)}$  can be expressed as the gradient of a lensing potential  $\psi^{(k)}$ :

$$\boldsymbol{\alpha}^{(k)}(\boldsymbol{\beta}^{(k)}) = \nabla_{\boldsymbol{\beta}^{(k)}} \psi^{(k)}(\boldsymbol{\beta}^{(k)}). \quad (9)$$

The differential deflection is then given by higher derivatives of the lensing potential. The second derivatives can be combined into the shear matrix

$$U_{ij}^{(k)} = \frac{\partial^2 \psi^{(k)}(\boldsymbol{\beta}^{(k)})}{\partial \beta_i^{(k)} \partial \beta_j^{(k)}} = \frac{\partial \alpha_i^{(k)}(\boldsymbol{\beta}^{(k)})}{\partial \beta_j^{(k)}}. \quad (10)$$

The lensing potential  $\psi^{(k)}$  is a solution of the Poisson equation:

$$\nabla_{\boldsymbol{\beta}^{(k)}}^2 \psi^{(k)}(\boldsymbol{\beta}^{(k)}) = 2\sigma^{(k)}(\boldsymbol{\beta}^{(k)}). \quad (11)$$

The dimensionless surface mass density  $\sigma^{(k)}$  is given by a projection of the matter distribution in a slice around lens plane:

$$\sigma^{(k)}(\boldsymbol{\beta}^{(k)}) = \frac{3H_0^2 \Omega_{\text{m}}}{2c^2} \frac{f_K^{(k)}}{a^{(k)}} \int_{w_{\text{L}}^{(k)}}^{w_{\text{U}}^{(k)}} dw' \delta_{\text{m}}(\boldsymbol{\beta}^{(k)}, w'). \quad (12)$$

Here,  $H_0$  denotes the Hubble constant,  $\Omega_{\text{m}}$  the mean matter density in terms of the critical density,  $f_K^{(k)} = f_K(w^{(k)})$  and  $a^{(k)} = a(w^{(k)})$ , with  $w^{(k)}$  denoting the line-of-sight comoving distance of the plane. Furthermore,  $\delta_{\text{m}}(\boldsymbol{\beta}^{(k)}, w')$  denotes the three-dimensional density contrast at comoving position  $(\boldsymbol{\beta}^{(k)}, w')$  relative to the mean matter density. The slice boundaries  $w_{\text{L}}^{(k)}$  and  $w_{\text{U}}^{(k)}$  have to satisfy  $w_{\text{L}}^{(k)} < w^{(k)} < w_{\text{U}}^{(k)}$  and  $w_{\text{U}}^{(k)} = w_{\text{L}}^{(k+1)}$ . They are usually chosen to correspond to the mean redshifts (e.g. Jain et al. 2000) or comoving distances (e.g. Wambsganss et al. 2004) of successive planes.<sup>7</sup> These conditions ensure that every region of the light cone contributes exactly to one lens plane, which is the closest plane in redshift or comoving distance.

Given the deflection angles on the lens planes, one can trace back a light ray reaching the observer from angular position  $\boldsymbol{\beta}^{(1)} = \boldsymbol{\theta}$  on the first lens plane to the other planes:

$$\boldsymbol{\beta}^{(k)}(\boldsymbol{\theta}) = \boldsymbol{\theta} - \sum_{i=1}^{k-1} \frac{f_K^{(i,k)}}{f_K^{(k)}} \boldsymbol{\alpha}^{(i)}(\boldsymbol{\beta}^{(i)}), \quad k = 1, 2, \dots \quad (13)$$

Here,  $f_K^{(i,k)} = f_K(w^{(k)} - w^{(i)})$ .

Equation (13) is not practical for tracing rays through many lens planes. An alternative expression is obtained as follows (see, e.g., Seitz et al. 1994, for a different derivation): The angular position  $\boldsymbol{\beta}^{(k)}$  of a light ray on the lens plane

<sup>7</sup> The exact choice for the projection boundaries becomes unimportant for sufficiently small spacings between the lens planes.

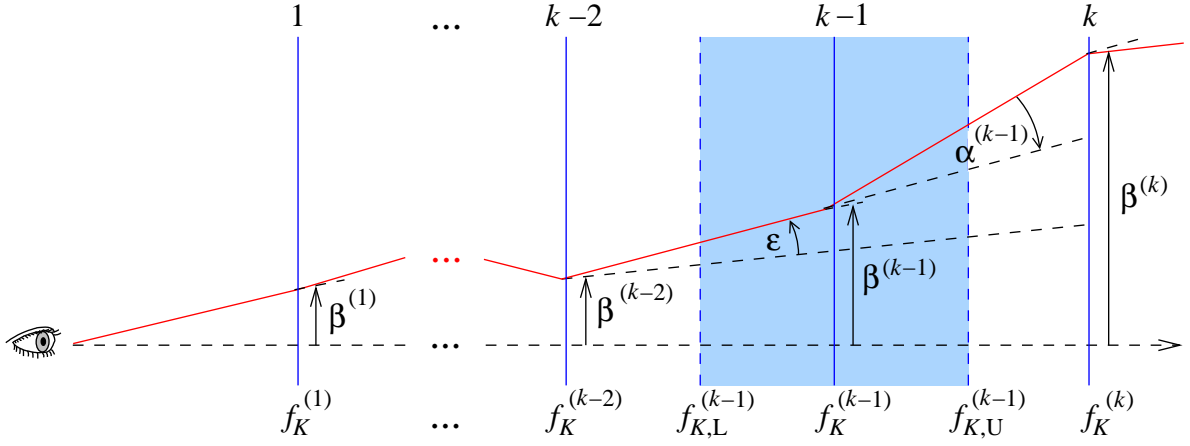


**Fig. 1.** Schematic view of the observer’s backward light cone in the multiple-lens-plane approximation. A light ray (red line) experiences a deflection only when passing through a lens plane (solid blue lines). The deflection angle  $\alpha^{(k-1)}$  of a ray passing through the lens plane at distance  $f_K^{(k-1)}$  from the observer is obtained from the matter distribution between  $f_{K,U}^{(k-1)}$  and  $f_{K,L}^{(k-1)}$  projected onto the plane. Using the deflection angle  $\alpha^{(k-1)}$  of the light ray at the previous lens plane and the ray’s angular positions  $\beta^{(k-1)}$  and  $\beta^{(k-2)}$  on the two previous planes, the angular position  $\beta^{(k)}$  on the current plane can be computed.

$k$  is related to its positions  $\beta^{(k-2)}$  and  $\beta^{(k-1)}$  on the two previous lens planes by (see Fig. 1):

$$f_K^{(k)} \beta^{(k)} = f_K^{(k)} \beta^{(k-2)} + f_K^{(k-2,k)} \epsilon - f_K^{(k-1,k)} \alpha^{(k-1)} (\beta^{(k-1)}), \quad (14)$$

$$\text{where } \epsilon = \frac{f_K^{(k-1)}}{f_K^{(k-2,k-1)}} (\beta^{(k-1)} - \beta^{(k-2)}).$$

Hence,

$$\begin{aligned} \beta^{(k)} = & \left( 1 - \frac{f_K^{(k-1)}}{f_K^{(k)}} \frac{f_K^{(k-2,k)}}{f_K^{(k-2,k-1)}} \right) \beta^{(k-2)} \\ & + \frac{f_K^{(k-1)}}{f_K^{(k)}} \frac{f_K^{(k-2,k)}}{f_K^{(k-2,k-1)}} \beta^{(k-1)} \\ & - \frac{f_K^{(k-1,k)}}{f_K^{(k)}} \alpha^{(k-1)} (\beta^{(k-1)}). \end{aligned} \quad (15)$$

For a light ray reaching the observer from angular position  $\theta$  on the first lens plane, one can compute its angular position on the other lens planes by iterating (15) with initial values  $\beta^{(0)} = \beta^{(1)} = \theta$ .

Differentiating (15) with respect to  $\theta$ , we obtain a recurrence relation for the distortion matrix:

$$\begin{aligned} \mathbf{A}_{ij}^{(k)} = & \left( 1 - \frac{f_K^{(k-1)}}{f_K^{(k)}} \frac{f_K^{(k-2,k)}}{f_K^{(k-2,k-1)}} \right) \mathbf{A}_{ij}^{(k-2)} \\ & + \frac{f_K^{(k-1)}}{f_K^{(k)}} \frac{f_K^{(k-2,k)}}{f_K^{(k-2,k-1)}} \mathbf{A}_{ij}^{(k-1)} \\ & - \frac{f_K^{(k-1,k)}}{f_K^{(k)}} \mathbf{U}_{ik}^{(k-1)} \mathbf{A}_{kj}^{(k-1)}. \end{aligned} \quad (16)$$

With the knowledge of the involved distances and shear matrices, this equation allows us to iteratively compute the

distortion matrix of a light ray from the observer to any lens plane. This equation requires in practice much fewer arithmetic operations and memory than the commonly used relations (e.g. by Jain et al. 2000) based on Eq. (13).

For comparison and testing, we will also use the multiple-lens-plane algorithm to calculate the distortion in the linear approximation by:

$$\mathbf{A}_{ij}^{(k)}(\theta) = \delta_{ij} - \sum_{n=1}^{k-1} \frac{f_K^{(n,k)}}{f_K^{(k)}} \mathbf{U}_{ij}^{(n)}(\theta). \quad (17)$$

### 3. The ray-tracing algorithm

The methods we use for ray-tracing through  $N$ -body simulations to study lensing are generally similar to those used by, e.g., Jain et al. (2000) or Vale & White (2003). First, the matter distribution on the past light cone of a fiducial observer is constructed from the simulation data. Then, the past light cone is partitioned into a series of redshift slices. The content of each slice is projected onto a lens plane. Finally, the multiple-lens-plane approximation is used to trace back light rays from the observer through the series of lens planes to the sources.

The aim of our ray-tracing algorithm is to make full advantage of the unprecedented statistical power offered by the large volume and high spatial and mass resolution of the Millennium Simulation. Therefore, our ray-tracing method differs in some important details from previous works. A brief outline of our algorithms for the construction of the past light cones and the lens planes has been given in an earlier work (Hilbert et al. 2007b). Here, we extend the discussion and provide a more detailed description.

#### 3.1. The Millennium Simulation

The Millennium Simulation (Springel et al. 2005) is a very large  $N$ -body simulation of cosmic structure formation in a flat  $\Lambda$ CDM universe. The following cosmological parameters were assumed for the simulation: a mat-

ter density of  $\Omega_m = 0.25$  in units of the critical density, a cosmological constant with  $\Omega_\Lambda = 0.75$ , a Hubble constant  $h = 0.73$  in units of  $100 \text{ km s}^{-1} \text{ Mpc}^{-1}$ , a spectral index  $n = 1$  and a normalization parameter  $\sigma_8 = 0.9$  for the primordial linear density power spectrum. These chosen parameters are consistent with the 2dF (Colless et al. 2003) and WMAP 1st-year data analysis (Spergel et al. 2003). The simulation was carried out with a customized version of GADGET-2 (Springel 2005). This code employed a TreePM algorithm with  $N = 2160^3$  particles of mass  $m_p = 8.6 \times 10^8 h^{-1} M_\odot$  to study the evolution of the matter distribution in a cubic region of  $L = 500 h^{-1} \text{ Mpc}$  comoving side length with periodic boundary conditions from redshift  $z = 127$  to the present. The force softening length was set to  $5 h^{-1} \text{ kpc}$  comoving.

The simulation data were stored on disk at 64 output times, which are spaced approximately logarithmically in expansion factor for  $z \geq 1$  and at roughly 200 Myr intervals between  $z = 1$  and the present. These snapshots contain, among other data, the positions, SPH smoothing lengths and friend-of-friend (FoF) group data of the particles. A special storage order was used for the particle data, which is based on the decomposition of the simulation cube into  $256^3$  smaller subcubes and a Peano Hilbert curve (see Springel 2005; Springel et al. 2005, for details). This storage order facilitates fast direct access to the particle data for small subvolumes of the simulation. In particular, the particle data for regions formed by iteratively subdividing the simulation cube into subcubes are contiguous blocks with their locations stored in a hashtable.

Complex physical processes of baryonic matter such as the formation and evolution of stars in galaxies has not been incorporated directly into the Millennium Simulation. However, several galaxy-formation models have been used to predict the properties of galaxies in the simulation (Springel et al. 2005; Croton et al. 2006; Bower et al. 2006; De Lucia & Blaizot 2007). The ray-tracing methods presented in this paper will allow us (in future work) not only to study Cosmic Shear in great detail, but also to make predictions for galaxy-galaxy lensing (and related higher-order statistics) for the various galaxy-formation models.

### 3.2. The construction of the matter in the backward light cones

Even with a comoving size of  $L = 500 h^{-1} \text{ Mpc}$ , the simulation box is too small to trace back light rays within one box. We therefore exploit the periodic boundary conditions of the simulation by arranging replicas of the simulation box in a simple cubic lattice with a lattice constant equal to the box size  $L$  to fill space. We refrain from randomly shifting or rotating the content of the lattice cells, because the simulation box is far too large to be projected onto a single lens plane. In addition, this allows us to keep the matter distribution continuous across the cell boundaries.

In this periodic matter distribution, light rays would encounter the same structures many times at different epochs before reaching relevant source redshifts if one chose the line of sight (LOS) parallel to the box edges. Hence, the LOS must be chosen at a skewed angle relative to the box axes. On the other hand, the application of Fourier methods for the calculation of the light deflection at the lens planes requires a matter density that is periodic perpendicular to

the LOS. Choosing a LOS parallel to  $\mathbf{n} = (n_1, n_2, n_3)$  with suitable coprime  $n_i \in \mathbb{Z}$ , one can obtain a large enough repetition length of  $|\mathbf{n}|L$  along the LOS (see Appendix A). At the same time, the matter distribution is periodic perpendicular to the LOS with an area of periodicity given by  $|\mathbf{n}|L^2$ . Our choice for  $\mathbf{n} = (1, 3, 10)$  yields a LOS periodicity of  $5.24 h^{-1} \text{ Gpc}$  (corresponds to  $z = 3.87$ ) and a rectangular unit cell of  $1.58 h^{-1} \text{ Gpc} \times 1.66 h^{-1} \text{ Gpc}$  for the lens planes. Moreover, any directions with shorter periodicity are at least  $1.81 \text{ deg}$  away from  $\mathbf{n}$ , and a light cone with a  $1.7 \text{ deg} \times 1.7 \text{ deg}$  field of view does not intersect with itself up to redshift  $z = 3.87$  when folded back into the simulation cube.<sup>8</sup> The resulting orientation of the LOS and the lens planes w.r.t. the simulation box are illustrated in Fig. 2.

We partition the observer's backward light cone into redshift slices such that each slice contains the part of the light cone that is closer in redshift to one of the snapshots than any other snapshot (with exceptions near the boundaries discussed below). The boundary between two redshift slices with snapshot redshifts  $z^{(k)}$  and  $z^{(k+1)}$  is thus a plane at comoving distance  $w_U^{(k)} = w_L^{(k+1)} = w [(z^{(k)} + z^{(k+1)})/2]$ . In addition,  $w_L^{(0)} = 0$ . The particle data of the snapshot closest in redshift is then used to approximate the matter distribution in each of these slices.

Because of the periodicity of the matter in the light cone, it suffices to construct the matter distribution in each redshift slice in a cuboid region that covers in projection one fundamental unit cell of the plane perpendicular to the chosen LOS. We utilize fast box-intersection tests (Gottschalk et al. 1996) and the special storage order of the simulation data in order to avoid reading and manipulation of the particle data as much as possible. Starting with all periodic copies of the simulation cube that potentially intersect with the slice, we determine whether (sub-)cubes are inside or outside the slice. If a cube is completely inside, the corresponding particle data is read and the particles are put directly into the slice. If a cube intersects partially with the slice, it is divided into eight subcubes and each subcube is considered in turn. Only if a subcube resulting from five subdivision is neither completely inside or outside, the particle positions of the corresponding region are checked individually.

In the construction of the matter distribution in the light cone, special care is taken for the particles near the boundary of two slices. In the simulation, particle concentrations representing dark matter halos of galaxies or clusters were identified by a friend-of-friend (FoF) group finding algorithm. Some of these halos are located on the slice boundaries with particles on either side. In order to avoid that such a halo is only partially included into a slice (and hence would be only partially projected onto a lens plane), a halo is either included as a whole if its central particle is inside the slice as defined by boundary planes, or completely excluded otherwise.

If the matter structure in the simulation were static, this procedure would suffice to prevent parts of the same halo from being projected onto adjacent lens planes, which

<sup>8</sup> We often use a larger field of view – in particular, if only lower source redshifts are considered. Even for high source redshifts, where the resulting light-cone may cover the same simulation region more than once, a large field of view can be used with due care (Hilbert et al. 2007a)

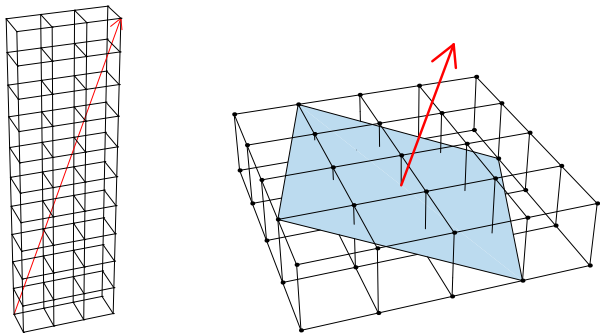


**Fig. 2.** Schematic view of the orientation of the line-of-sight (red line) and the lens planes (blue area) relative to the simulation box (indicated by black lines).

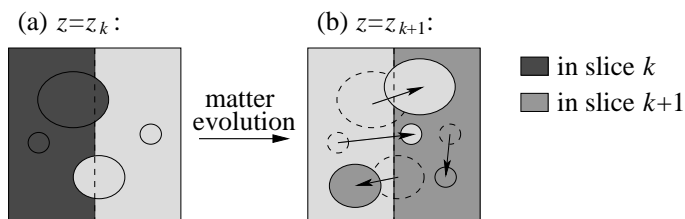


**Fig. 3.** Schematic view of the adaptive slice boundaries to avoid the truncation or double inclusion of halos that are located near a slice boundary. Halos near the boundary of slice  $k$  and  $k+1$  are either included as a whole in slice  $k$  or completely excluded depending on the positions of their centres (a). Halos that are included (excluded) in slice  $k$ , are excluded (included) from slice  $k+1$  even if they have crossed the slice boundary between redshift  $k$  and  $k+1$  (b).

would create artificial close pairs of halos on the sky. Halos, however, may have moved across a slice boundary between two snapshots. We therefore amend the above inclusion criterion for halos near the boundary: If a halo is included in (excluded from) the slice of the later snapshot, its progenitors in the earlier snapshot are excluded from (included in) the ‘earlier’ slice even if their centres lie on the ‘early’ (‘late’) side of the slice boundary. These inclusion criteria for halos are illustrated in Fig. 3.

### 3.3. The lens planes

The matter content of each redshift slice of the backward light cone is projected along the LOS direction onto a lens plane. Each lens plane is placed at the comoving distance of the corresponding snapshot’s redshift. The lens planes serve also as source planes for the ray-tracing. The resulting number of lens planes as a function of the source redshift is shown in Fig. 4.

The light deflection angles and distortions resulting from the projected matter density on the lens planes are computed by particle-mesh (PM) methods. Mesh methods have the advantage that, once the deflection and distortion are computed on a mesh (e.g. by Fourier methods), the computation of the deflections and distortions for many light rays intersecting the plane is very fast. One of its disadvantage is that the mesh spacing used limits the spatial resolution of the projected matter distribution. However, any  $N$ -body simulation providing the matter dis-

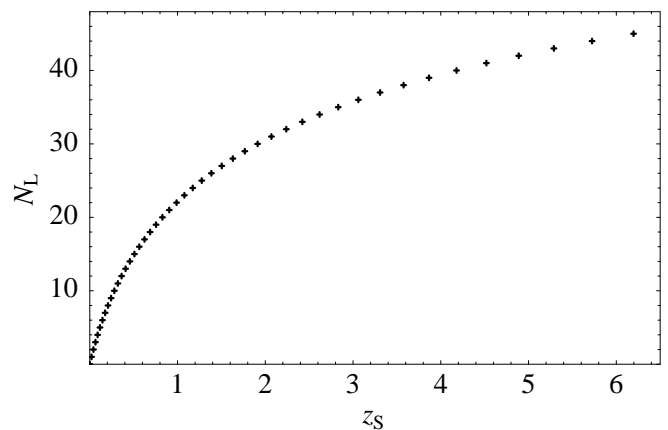


**Fig. 4.** The number  $N_L$  of lens planes used for the ray-tracing as a function of the source redshift  $z_s$ .

tribution for the ray-tracing has a limited resolution as well. In dense regions, the spatial resolution of the Millennium Simulation is effectively determined by the force softening, which is  $5h^{-1}$  kpc comoving. Thus, a mesh spacing of  $2.5h^{-1}$  kpc comoving is required to avoid resolution degradation for the projected matter density. However, a single mesh covering the full periodic area of the lens plane (i.e.  $1.58h^{-1}$  Gpc  $\times$   $1.66h^{-1}$  Gpc comoving) with such a small mesh spacing would be too demanding, in particular regarding the memory required both for its computation and storage. We therefore use a hierarchy of meshes instead.

The lensing potential  $\psi$  is split into a long-range part  $\psi_{\text{long}}$  and a short-range part  $\psi_{\text{short}}$ . The split is defined in Fourier space by:

$$\tilde{\psi}_{\text{long}}(\ell) = \tilde{\psi}(\ell) \exp(-\beta_{\text{split}}^2 \ell^2), \quad \text{and} \quad (18)$$

$$\tilde{\psi}_{\text{short}}(\ell) = \tilde{\psi}(\ell) [1 - \exp(-\beta_{\text{split}}^2 \ell^2)]. \quad (19)$$

The splitting angle  $\beta_{\text{split}} = r_{\text{split}}/f_K(w)$ , with comoving splitting length  $r_{\text{split}}$  and comoving angular diameter distance of the lens plane  $f_K(w)$ , quantifies the spatial scale of the split. Different meshes are then used to calculate  $\psi_{\text{long}}$  and  $\psi_{\text{short}}$ .

First, the particles in each slice are projected onto a coarse mesh of  $16384 \times 16384$  points covering the whole periodic area of the lens plane using clouds-in-cells (CIC) assignment (Hockney & Eastwood 1981). The long-range potential  $\psi_{\text{long}}$  is then calculated on this mesh by means of fast Fourier transform (FFT) techniques (Cooley & Tukey 1965; Frigo & Johnson 2005). The splitting length  $r_{\text{split}} = 175h^{-1}$  kpc is chosen slightly larger than the coarse mesh spacing ( $96h^{-1}$  kpc and  $101h^{-1}$  kpc comoving, respectively), so the coarse mesh samples  $\psi_{\text{long}}$  with sufficient accuracy. For each lens plane, the long-range potential is calculated once, and the result is stored on disk for later use during the ray-tracing.

The short-range potential  $\psi_{\text{short}}$  is calculated ‘on the fly’, i.e. during the actual ray-tracing. The area where the light rays intersect the plane is determined and, if larger than  $40h^{-1}$  Mpc comoving, subdivided into several patches up to that size. Each patch is covered by a fine mesh with a mesh spacing of  $2.5h^{-1}$  kpc comoving and up to  $16384 \times 16384$  mesh points. The fine meshes are chosen slightly larger than the patches in order to take into account all matter within the effective range of  $\psi_{\text{short}}$ , for which we

assume  $875h^{-1}$  kpc ( $= 5r_{\text{split}}$ ). Since the fine mesh is chosen large enough, mesh points close to its boundary are not used in the subsequent analysis. Periodic boundary conditions can therefore be used for the FFT on the patches without ‘zero padding’.

In order to reduce the shot noise from the individual particles, either a fixed or an adaptive smoothing scheme is used for the matter distribution on the fine meshes. In case of the fixed smoothing, the particles in the slice are projected onto the fine mesh using CIC. The resulting matter density on the fine mesh is then smoothed in Fourier space by applying Gaussian low pass filter with a kernel

$$K_s(\boldsymbol{\ell}; \beta_s) = \frac{1}{2\pi\beta_s^2} \exp\left(-\frac{\ell^2}{2\beta_s^2}\right) \quad (20)$$

whose filter-scale  $\beta_s = l_s/f_K(w)$  is determined by the lens plane’s comoving distance  $w$  and a fixed comoving filter scale  $l_s$ . This is done during the calculation of the short-range potential  $\psi_{\text{short}}$  with FFT methods.

In case of the adaptive smoothing, the mass associated with each simulation particle contributes

$$\Sigma_p(\mathbf{x}) = \begin{cases} \frac{3m_p}{\pi r_p^2} \left(1 - \frac{|\mathbf{x} - \mathbf{x}_p|^2}{r_p^2}\right)^2, & |\mathbf{x} - \mathbf{x}_p| < r_p, \\ 0, & |\mathbf{x} - \mathbf{x}_p| \geq r_p, \end{cases} \quad (21)$$

to the surface mass density on the fine mesh. Here,  $\mathbf{x}$  denotes comoving position on the lens plane,  $\mathbf{x}_p$  is the projected comoving particle position, and  $r_p$  denotes the comoving distance to the 64th nearest neighbor particle in *three* dimensions (i.e. before projection). The adaptive smoothing is essentially equivalent to the assumption that, in three-dimensional space, each simulation particle represents a spherical cloud with a Gaussian density profile and an *rms* radius that is half the distance to its 64th nearest neighbor. From the resulting surface mass density on the fine mesh, the short-range potential  $\psi_{\text{short}}$  is then calculated by FFT methods.

The long- and short-range contributions to the deflection angles and shear matrices are calculated on the coarse and fine mesh by finite differencing of the potentials. The values between mesh points are obtained by bilinear interpolation. The resulting deflection angles and shear matrices at the ray positions are then used to advance the rays and their associated distortion matrices from one plane to the next.

The ray-tracing algorithm reproduces the deflection angles and distortions caused by a single point mass very accurately, as is shown in Fig. 5 and 6. For the deflection angle, the relative deviation from the known analytical result is at most one percent, with a much smaller rms error. Apart from scales below  $10h^{-1}$  kpc comoving, where discreteness of the fine mesh becomes important, the largest relative errors occur on the scale of the split between short- and long-range potential. If desired, an even smaller error in this region could be obtained by increasing the splitting scale.

In this work, we do not consider the effects of the stellar mass in galaxies. Note, however, that the ray-tracing algorithm can be extended to include the gravitational effects of the stars in galaxies as described in Hilbert et al. (2008): The positions and stellar masses of the galaxies are

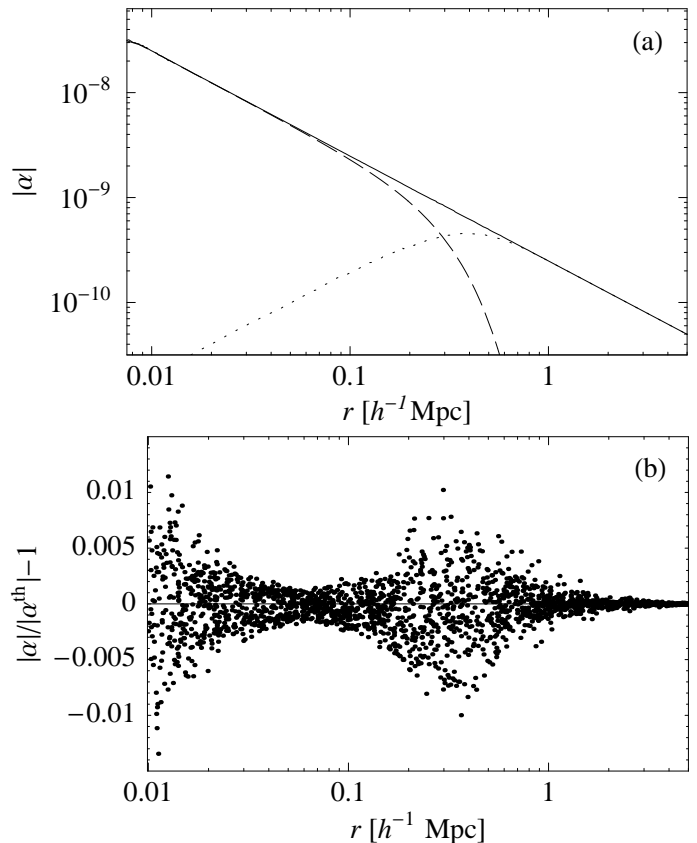


**Fig. 5.** The deflection angle  $|\alpha|$  as a function of the comoving distance  $r$  to a point mass computed by our mesh method. (a) Short-range component (dashed line) and long-range component (dotted line) of the deflection angle (full line). (b) Fractional difference between the value  $\alpha$  calculated by our mesh method and the theoretical value  $\alpha^{\text{th}}$ . For the plots, we placed 10 point masses of  $8.6 \times 10^8 h^{-1} M_{\odot}$  randomly on the lens plane at  $z = 0.5$  and calculated the resulting deflection at 1000 randomly positions around each of them.

inferred from semi-analytic galaxy-formation models implemented within the evolving dark-matter distribution of the Millennium Simulation (Springel et al. 2005; Croton et al. 2006; De Lucia & Blaizot 2007). The light deflection induced by the stellar matter is then calculated using analytic expressions for the projected stellar mass profiles on the lens planes. The error made by adding the stellar matter onto the lens planes, although the dark-matter particles of the simulation represent the *total* matter, can then be compensated using extended analytic profiles with negative masses.

### 3.4. Lensing maps and image positions

To produce lensing maps, we set up rays starting from a fiducial observer on a regular grid in the image plane with an angular field size and resolution suitable for the particular application. The resulting shear and convergence maps may be used directly to obtain, e.g., the shear correlation functions and power spectra.

We also wish to perform simulations of galaxy-galaxy lensing. Not only are the image positions of distant ‘source’ galaxies affected by lensing. Also the apparent positions of

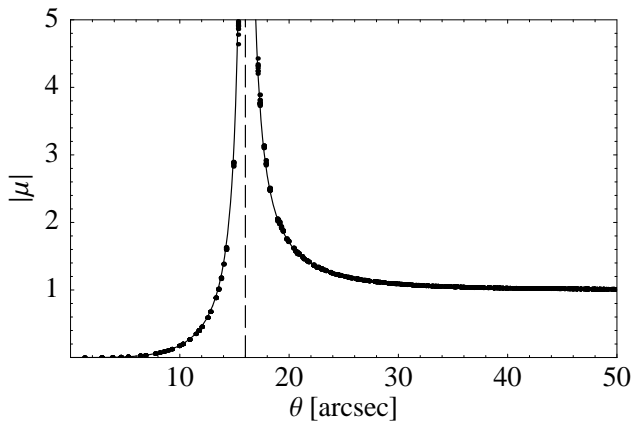


**Fig. 6.** The magnification  $|\mu|$  for sources at  $z = 2$  as a function of the angular separation  $\theta$  to a point mass of  $10^{14}h^{-1}M_{\odot}$  at redshift  $z = 1$  computed by our mesh method. The numerical values (points) are compared to the analytical result (solid line). The magnification diverges at the Einstein radius  $\theta_E = 16''$  (dashed vertical line).

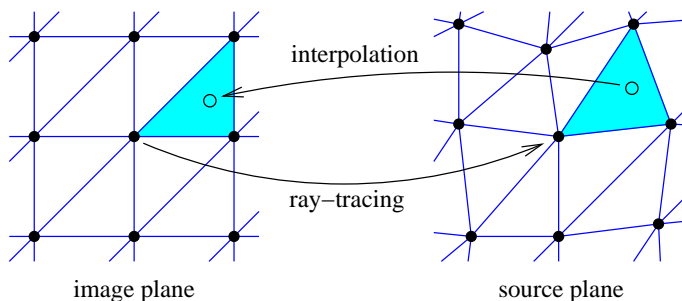


**Fig. 7.** Interpolation scheme used for determining image positions of galaxies. The regular grid of rays in the image plane (left filled circles) is used to partition the image plane into triangles (right blue lines). The image position (left open circle) of a source inside a triangle (right blue lines) formed by the backtraced rays on the source plane (right filled circles) is then determined by linear interpolation.

galaxies and halos that act as lenses for background galaxies (and are to be correlated with the shear field) are affected by lensing due to foreground matter. We therefore have to compute the image positions  $\theta_g$  given the galaxies' source positions  $\beta_g^{(k)}$  (i.e. the projected galaxy positions on the lens planes) and the lens mapping sampled on the grid of light rays in the ray-tracing algorithm. To reach this, we make use of a triangle technique described, e.g., in Schneider et al. (1992). We partition the region of the image plane that is covered by the grid of rays into triangles formed by rays of adjacent grid points (see Fig. 7). On each lens plane, we identify for each such triangle all galaxies with source position inside the backtraced triangle. The image positions of these galaxies are then computed by linear interpolation between the rays. This method takes into account strong lensing, as a galaxy might lie in more than one triangle on the lens plane. As a result, there are multiple images of such a galaxy.

Figure 8 illustrates how well the image positions obtained by the triangle interpolation method are mapped back onto the known source positions by the ray-tracing. Shown is the difference between the known source positions

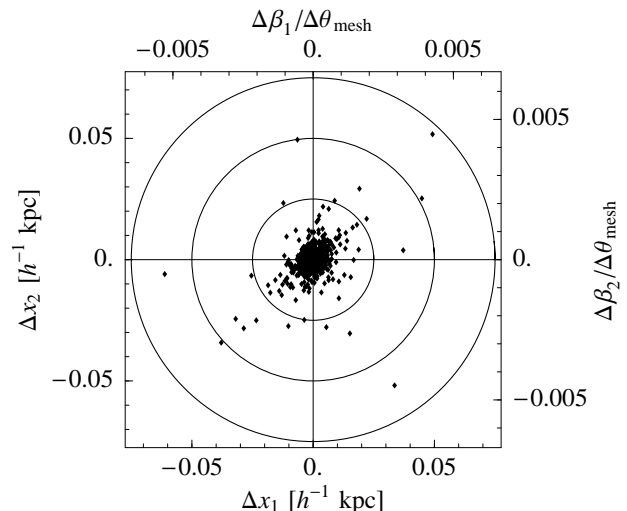


**Fig. 8.** Comparison of the known source positions and the source positions obtained by tracing back light rays starting from the image positions computed by the interpolation method. Shown is the difference between ‘true’ and ‘traced back’ comoving source position  $\Delta\mathbf{x}$  for 1000 galaxy centres at  $z = 1$ . At this redshift,  $0.010h^{-1}$  kpc comoving correspond to an angle of  $10^{-3}$  arcsec. The right and upper frame sides are labelled by the difference of the ‘true’ and ‘traced back’ source angle  $\Delta\beta$  in units of the mesh spacing  $\Delta\theta_{\text{mesh}} = 1''$  used for the rays.

and the source positions obtained by tracing back light rays starting from the interpolated image positions. The difference is always much smaller than the resolution of the matter distribution on the lens planes. The slight anisotropy seen as a larger spread along one diagonal is caused by the particular way the image plane was partitioned into triangles. The diagonal coincides with the diagonal chosen for splitting the square mesh pixels into triangles. If one used the other diagonal for splitting the mesh pixels into triangles, a larger spread along that diagonal would be seen instead.

## 4. Results

We compute various weak-lensing two-point statistics from a set of ray-tracing simulations and compare the results to semi-analytic predictions.

### 4.1. Power spectra

We start our discussion with the convergence power spectrum  $P_{\kappa}(\ell)$ . In the linear approximation, the convergence power spectrum is given by (see, e.g., Schneider 2006):

$$P_{\kappa}(\ell) = \frac{9H_0^4\Omega_m^2}{4c^2} \int_0^{\infty} dw \frac{q^2(w)}{a^2(w)} P_{\delta} \left( t(w), \frac{\ell}{f_K(w)} \right). \quad (22)$$

Here,

$$q(w) = \int_w^{\infty} dw' p_s(w') \frac{f_K(w' - w)}{f_K(w)}, \quad (23)$$

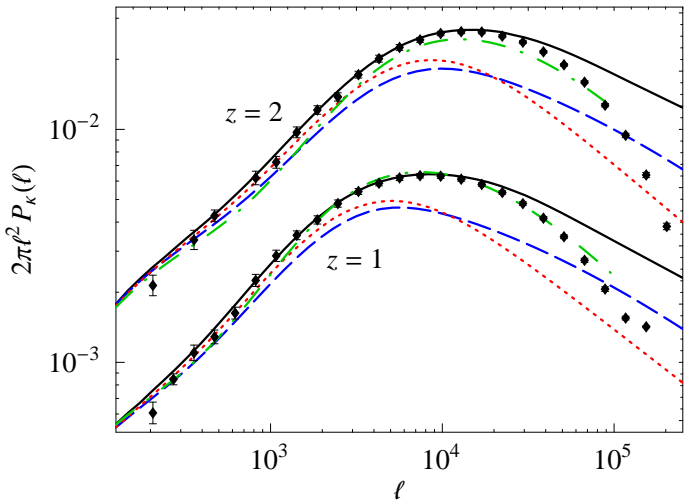


**Fig. 9.** Convergence power spectra  $P_\kappa(\ell)$  for sources at redshift  $z = 1$  (lower curves) and  $z = 2$  (upper curves). The simulation results (from  $\sim 30$  random fields of  $3 \times 3 \text{ deg}^2$ ) are shown as diamonds with errorbars (indicating the field-to-field variance), the corresponding linear predictions as solid lines. The predictions using the Peacock & Dodds (1996) prescription together with the transfer function from Eisenstein & Hu (1999) are given as dotted lines, those obtained from the Smith et al. (2003) fitting formula as dashed lines. The predictions of a halo model using the concentration parameters of Neto et al. (2007) are shown as dash-dotted lines.

with the probability distribution  $p_s(w)$  of visible sources in comoving distance. Furthermore,  $P_\delta(t, k)$  denotes the three-dimensional power spectrum of the matter contrast  $\delta$  at cosmic time  $t$  and comoving wave vector  $k$ . For an accurate comparison with the results obtained by our ray-tracing algorithm, we use Eq. 22 together with the three-dimensional power spectra  $P_\delta(k)$  measured from the Millennium Simulation (see also Vale & White 2003). In the following, we will call the resulting power spectra *linear prediction* for brevity.

In Fig. 9, we compare the linear prediction to the convergence power spectra obtained from the ray-tracing. As has already been observed by Jain et al. (2000) and Vale & White (2003), the power spectra from the ray-tracing are in very good agreement with the linear prediction. For the considered source redshifts, the difference  $\lesssim 2\%$  for  $\ell < 10^4$ . The larger deviations at wave numbers  $\ell > 2 \times 10^4$  are due to smoothing effects discussed below.

In the linear approximation, the power spectra of the convergence and the shear are identical. As has already been found, e.g., by Jain et al. (2000), the convergence and shear power spectra from ray-tracing agree very well, too. On scales  $\ell > 1000$ , the difference between both is well below one percent in our ray-tracing results.

The comparison of the ray-tracing power spectra with some of the popular fitting formulae is less encouraging: Both the prescriptions by Peacock & Dodds (1996) (with the transfer function by Eisenstein & Hu 1999) and Smith et al. (2003) strongly underpredict the power on intermediate and small scales. These fitting formulae are based on older simulations, whose matter power spectra are noticeably different from the power spectra of more

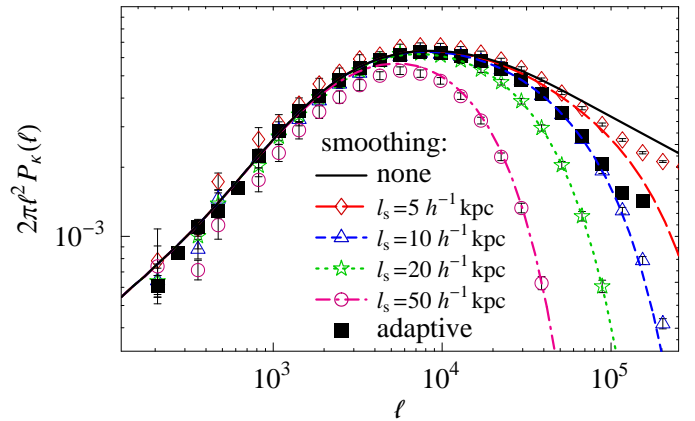


**Fig. 10.** Convergence power spectra  $P_\kappa(\ell)$  for sources at redshift  $z = 1$ . Compared are the results from ray-tracing (open and filled symbols) using various smoothing schemes (none/Gaussian with fixed scale  $l_s$ /adaptive) and the corresponding linear prediction (lines) obtained projecting and smoothing the measured 3D power spectra of the actual mass distribution in the simulation.

recent, higher-resolution simulations. The deviations from the simulated convergence power spectra exceed 30% for  $\ell > 10000$ , so these fitting formulae seem to be of limited use for the interpretation of data from future weak-lensing surveys.

A prediction based on the popular halo model (Seljak 2000; Cooray & Sheth 2002) and the halo concentration-mass relation of Neto et al. (2007) provides a better fit to the convergence power spectrum. There are, however, still deviations ( $\approx 10\%$ ), most notably for intermediate scales of  $\ell \approx 1 - 2 \times 10^3$ . This coincides with the transition region of the one- and two-halo terms, which is difficult to model accurately due to halo exclusion effects (see e.g. Tinker et al. 2005, and references therein) which we did not include in our prediction.

In Fig. 10, we present the convergence power spectra from ray-tracing runs of the same set of fields (with a cumulative area of  $80 \text{ deg}^2$  and sources at  $z = 1$ ), but with different smoothing schemes. In addition to adaptive smoothing, which is intractable analytically, we also employ smoothing with a Gaussian kernel of fixed comoving size on the lens planes. The ray-tracing simulations with Gaussian smoothing on the lens planes show – apart from sampling variance – perfect agreement with the linear prediction if the smoothing is into account there. Only the spectrum for the smallest smoothing length shows some aliasing effects on very small scales. The spectrum of the adaptive-smoothing runs happens to match the spectrum for a Gaussian smoothing length of  $10h^{-1} \text{ kpc}$  comoving quite well, but one should be cautious when considering this as an “effective” smoothing length in a different context.

#### 4.2. Aperture-mass statistics

A suitable cosmic-shear measure that allows one to decompose the shear signal in a finite-sized field into E- and B-modes is the aperture mass dispersion (Schneider et al. 1998, 2002). The E- and B-mode aperture mass at position

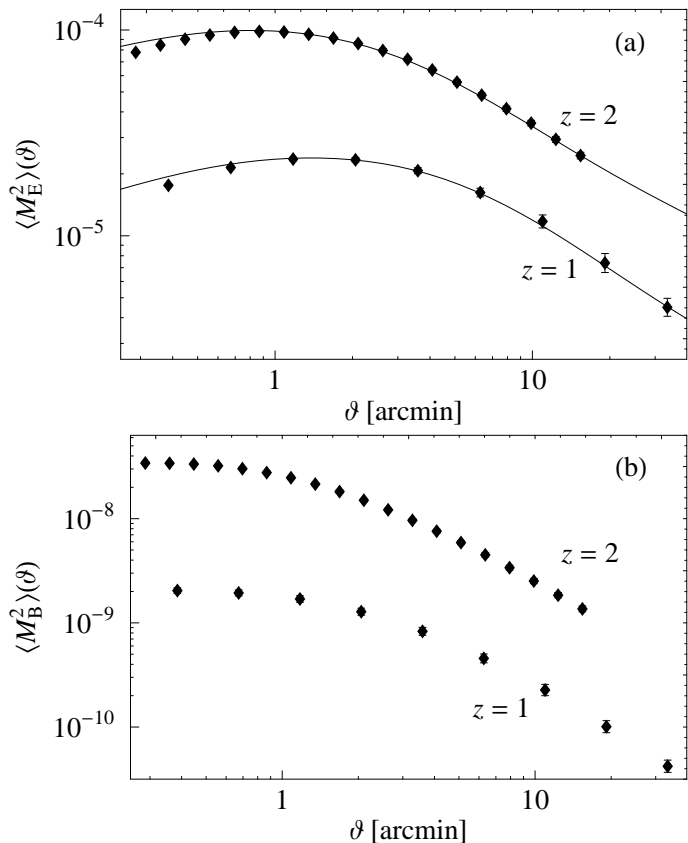


**Fig. 11.** Aperture mass dispersion  $\langle M_E^2 \rangle$  (a) and  $\langle M_B^2 \rangle$  (b) for sources at  $z = 1$  and  $z = 2$ . Compared are the linear prediction (solid lines, E-mode only) and the results from ray-tracing (symbols).

$\theta$  on the sky and scale  $\vartheta$  are defined by:

$$M_{E,B}^2(\theta, \vartheta) = \int d^2\theta' Q(\theta' - \theta, \vartheta) \gamma_{t,\times}(\theta', \theta' - \theta), \quad (24)$$

In this work we use the polynomial filter function  $Q$  proposed by Schneider et al. (1998):

$$Q(\theta, \vartheta) = \frac{6|\theta|^2}{\pi\vartheta^4} \left(1 - \frac{|\theta|^2}{\vartheta^2}\right). \quad (25)$$

The tangential and cross components of the shear are defined by

$$\gamma_t(\theta', \theta) = -\Re\left(\gamma(\theta')e^{-2i\phi(\theta)}\right), \quad (26a)$$

$$\gamma_\times(\theta', \theta) = -\Im\left(\gamma(\theta')e^{-2i\phi(\theta)}\right), \quad (26b)$$

where  $\phi(\theta)$  is the polar angle for the direction defined by  $\theta$ .

An estimate for the aperture mass dispersion  $\langle M_{E,B}^2 \rangle(\vartheta)$  as a function of the filter scale  $\vartheta$  can be computed from a given shear field by a spatial average. Figure 11a shows the E-mode aperture mass dispersion measured from our set of simulations. The dispersion measured from the ray-tracing is in very good agreement with the linear prediction (Schneider et al. 1998):

$$\langle M_E^2 \rangle(\vartheta) = \frac{288}{\pi} \int_0^\infty d\ell \frac{\ell J_4^2(\vartheta\ell)}{(\vartheta\ell)^4} P_\kappa(\ell), \quad (27)$$

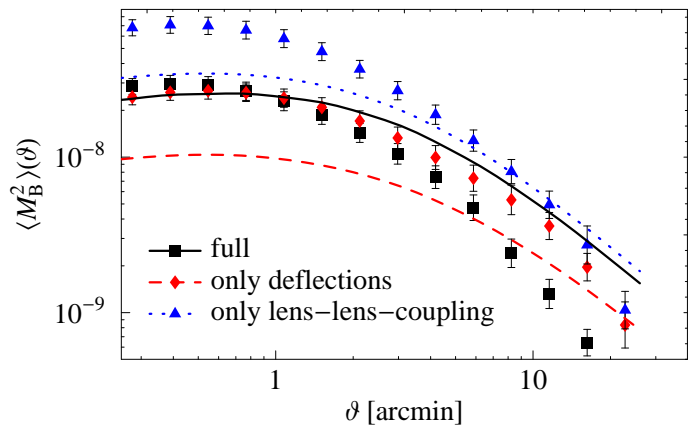


**Fig. 12.** B-mode aperture mass dispersion  $\langle M_B^2 \rangle$  for sources at  $z = 2$  decomposed into the contributions by lens-lens-coupling and ray deflections. Compared are the results from ray-tracing (symbols) and the predictions based on Cooray & Hu (2002) (lines).

where  $P_\kappa(\ell)$  is given by Eq. (22), and  $J_4$  denotes a Bessel function of the first kind.

In the linear approximation, the B-mode aperture mass dispersion  $\langle M_B^2 \rangle(\vartheta)$  vanishes. The measured B-mode dispersion from the full ray-tracing is shown in Fig. 11b. The B-mode signal is at least 3 orders of magnitude smaller than the E-mode. On larger scales their ratio even drops below  $10^{-5}$ .

Theoretical predictions of the amplitude of the lensing-induced B-modes have been made by Cooray & Hu (2002), who calculated the corrections to the power spectra of E- and B-modes up to fourth order in the gravitational potential by expanding (4) to higher than the usual first order. As Fig. 12 illustrates, the predictions based on their method (and the measured three-dimensional power spectra of the Millennium Simulation) are of the correct order of magnitude and reproduce some qualitative features of the ray-tracing simulations, but the match is far from being perfect. While the B-mode prediction is lower by a factor of  $\approx 2$  on small scales, the signal measured from the ray-tracing declines much more quickly on larger scales. However, the discrepancies are not large enough to challenge the finding of Shapiro & Cooray (2006) that the lensing-induced B-mode is unimportant even for an all-sky survey.

In order to determine their individual contributions to the total B-mode signal, we switch off ray-deflections [i.e. we employ the Born approximation by setting  $\theta^{(k)} = \theta \forall k$  in Eq. (15)] and/or lens-lens-coupling [i.e. we set  $A^{(k-1)} = 1$  in the third term on the r.h.s. of Eq. (16)]. Again the predictions and the measured signal differ by factors  $\sim 2$  on small scales, and the measured signal decreases much stronger with increasing scale.

In order to exclude numerical artifacts as the reason for the discrepancy, we closely examined various steps involved in the calculations: The results did not change when different ways of estimating  $M_B^2$  in real and Fourier space, as well as different methods of numerical integration for the theoretical curves were used. Furthermore, only a tiny B-mode (at least 6 orders of magnitudes smaller than the E-mode) remained, when both ray deflections and lens-lens-coupling were switched off in the simulation (which is essentially equivalent to the linear approximation). The origin of this

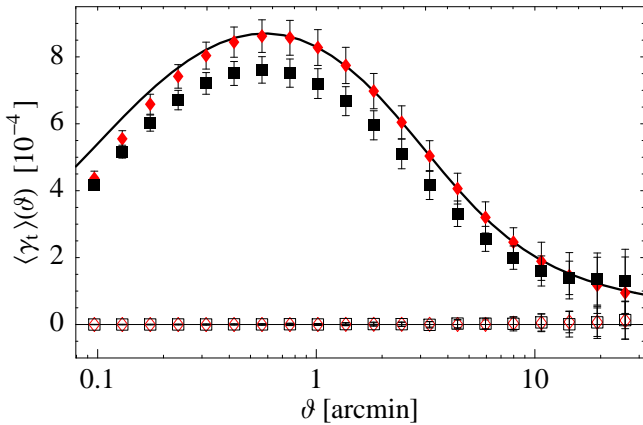


**Fig. 13.** Galaxy-galaxy-lensing signal for sources at redshift  $z = 1$  and unbiased lens galaxies with a constant comoving mean density between  $z = 0$  and  $z = 1$ . Shown are the measured tangential component  $\langle \gamma_t \rangle(\vartheta)$  (filled symbols) and cross component  $\langle \gamma_{\times} \rangle(\vartheta)$  (open symbols) of the shear from full ray-tracing (squares) and ray-tracing using the linear approximation (17) (diamonds), and the linear prediction (28) (solid line).

tiny signal is found to be the interpolation of the Jacobian matrix between the grid points to obtain their values at the light ray positions. Sampling a B-mode free, continuous shear field on a grid and subsequent interpolation yields again a continuous shear field. This, however, agrees exactly with the original field only at the grid points. Therefore, it may in general contain a small B-mode contribution, depending on the grid resolution and the interpolation scheme used.

### 4.3. Galaxy-galaxy lensing

We test the effect of Born corrections and lens-lens coupling on galaxy-galaxy lensing (GGL) by producing a catalog of unbiased mock galaxies. We achieve this by first drawing a number of simulation particles on each lens plane at random and using their positions as lens galaxy positions in the algorithm described in Sec. 3.4. We then obtain a catalog of source galaxies by randomly sampling the shear fields obtained during the ray-tracing.

The GGL signal we are interested in is given by the mean tangential shear  $\langle \gamma_t \rangle(\vartheta)$  at the image positions of the source galaxies as a function of angular separation  $\vartheta$  to the positions of the lens galaxies. In the simple case of unbiased galaxies considered here, the expected GGL signal can be computed in the linear approximation by:

$$\langle \gamma_t \rangle(\vartheta) = \frac{1}{2\pi} \int dw \frac{p_1(w)q(w)}{a(w)f_K(w)} \times \int d\ell J_2(\vartheta\ell) P_\delta \left( t(w), \frac{\ell}{f_K(w)} \right), \quad (28)$$

where  $J_2$  is a Bessel function of the first kind,  $p_1(w)$  is the probability distribution of the lens galaxies' distances, the lensing weight  $q(w)$  is given by Eq. (23), and  $P_\delta$  denotes again the 3D matter power spectrum. For simplicity, we will consider a volume-limited sample of lens galaxies with constant comoving density in the following.

Due to statistical parity invariance, the cross component  $\gamma_{\times}$  is expected to vanish when averaged over many source-lens pairs. The observed mean cross component  $\langle \gamma_{\times} \rangle$  can therefore be used as a test for systematic effects and “cosmic variance”. As shown in Fig. 13,  $\langle \gamma_{\times} \rangle$  is consistent with zero in our ray-tracing.

While the cross component  $\gamma_{\times}$  provides a test for systematic effects, the tangential shear  $\gamma_t$  contains the desired information about the matter and galaxy distribution. As can be seen in Fig. 13, the mean tangential shear  $\langle \gamma_t \rangle$  is significantly smaller ( $\approx 10 - 20\%$  at an angular separation of 1 arcmin) in the ray-tracing than expected from the linear prediction (28).

The reason for this discrepancy is magnification bias: Lenses, i.e. dense matter structures such as galaxies or clusters with their dark matter halos, magnify the regions behind them. The magnification reduces the apparent number density of higher-redshift lens galaxies around lower-redshift lenses in a volume limited survey (as has been simulated here). Underdense regions, on the other hand, demagnify the regions behind them, thereby increasing the apparent number density of lens galaxies behind them. The de-/magnification leads to an anticorrelation between the positions of high-redshift lens galaxies and the tangential shear induced by low-redshift structures. The anticorrelation reduces the signal  $\langle \gamma_t \rangle$  compared to the linear approximation.<sup>9</sup> We can suppress the magnification bias in the ray-tracing by switching off the deflections and using Eq. (17) to calculate the distortions. In this case our simulations are fully consistent with the linear prediction, as is shown in Fig. 13.

The effect of the magnification bias on the GGL depends on the redshift distribution of the sources and the lenses. Moreover, the shape of the lens luminosity function may be important if the lens population is selected using a magnitude limit. For example, the linear approximation may *underestimate*  $\langle \gamma_t \rangle$  for a lens population with a very steep luminosity function near the survey magnitude limit. We reserve a more detailed investigation of this effect with realistic source and lens distributions for future work.

## 5. Summary

In this work, we have described a new variant of the multiple-lens-plane algorithm, which is particularly suited for ray-tracing through very large cosmological  $N$ -body simulations. The algorithm differs in some important details from previous works. This allows us to take full advantage of the unprecedented statistical power offered by the large volume and high spatial and mass resolution of the Millennium Simulation. The features discussed include: a tilted line-of-sight (to avoid periodic repetition of structures along the line-of-sight), adaptive slice boundaries (to avoid the slicing and duplication of bound structures), adaptive smoothing of the projected matter distribution on the lens planes (to reduce shot noise from the particles), a mutli-mesh method for calculating the light deflections and distortions at the lens planes (which takes into account the small-scale and large-scale structure simultaneously), and

<sup>9</sup> Note that in the linear approximation, magnification effects are neglected. Thus, the positions of galaxies at any given redshift are uncorrelated with the shear induced by galaxies at different redshifts.

a method to include galaxies (as lenses and sources) from semi-analytic galaxy-formation models in the ray-tracing process.

We have used the ray-tracing code and the Millennium Simulation to investigate the impact of lens-lens coupling and multiple ray deflections on various cosmic shear two-point statistics. We have computed convergence power spectra from a set of ray-tracing realizations. For testing and comparison, we have also computed a linear prediction of the convergence power spectrum using the measured three-dimensional power spectra of the mass distribution in the Millennium Simulation. We find that this linear prediction agrees very well with the ray-tracing results except for very small scales (the difference is  $> 5\%$  only for  $\ell > 20000$ ), where smoothing on the lens planes becomes important.

Comparing the convergence power spectrum from the ray-tracing to the predictions based on the fitting formulae for the matter power spectrum by Peacock & Dodds (1996) and Smith et al. (2003), we find significant discrepancies ( $> 30\%$  for  $\ell > 10000$ ), casting the usefulness of these fitting formulae for cosmological parameter estimation for future surveys into doubt. A prediction based on the popular halo model and the halo concentration-mass relation of Neto et al. (2007) fits better, but there are still noticeable deviations, in particular for higher source redshifts ( $\sim 10\%$  for sources at  $z^S = 2$ ). This indicates a need for more accurate descriptions of matter power spectra.

Furthermore, we have computed the E- and B-mode aperture mass dispersion using our ray-tracing algorithm. We find the B-mode to be finite, but at least three orders of magnitude smaller than the E-mode. The amplitude of the B-mode is slightly larger and shows a different scale dependence than the prediction of Cooray & Hu (2002). We have performed various tests to exclude numerical artifacts as the origin of the deviations. Despite these discrepancies, we can confirm the finding of Shapiro & Cooray (2006) that the lensing-induced B-mode can be safely neglected even in an all-sky survey.

Corrections to the linear approximation can have a considerable impact on galaxy-galaxy lensing. In the simple case of a volume-limited sample of unbiased lens galaxies and all sources at redshifts  $z = 1$ , the linear approximation overestimates the mean tangential shear around lenses by  $\approx 10 - 20\%$  at an angular separation of 1 arcmin due to its failure to incorporate the magnification bias. The impact of the magnification bias on the galaxy-galaxy lensing signal depends on the survey selection criteria and the luminosity and redshift distribution of the sources and the lenses. A detailed investigation of this effect should be carried out in future work.

*Acknowledgements.* We thank Volker Springel, Jeremy Blaizot, Ole Möller, Martin Kilbinger and Emilio Pastor-Mira for helpful discussions, and Jasmin Pielorz for providing the halo model power spectra. This work was supported by the DFG within the Priority Programme 1177 under the projects SCHN 342/6 and WH 6/3.

## Appendix A: Lattice planes

The periodicity of our matter distribution along and perpendicular to the line-of-sight can be studied within the theory of crystal lattices (see, e.g., Ashcroft & Mermin 1976). Here, we give a practical explanation rather than a rigorous proof.

Consider an array of unit cubes forming a simple cubic lattice with lattice constant unity. Choose two linearly independent lattice vectors  $\mathbf{p}$  and  $\mathbf{q}$  with  $\mathbf{p} = (p_1, p_2, p_3)$  and  $\mathbf{q} = (q_1, q_2, q_3)$  and  $p_i, q_i \in \mathbb{Z}$ . These two vectors span a plane which is perpendicular to the lattice vector  $\mathbf{n}$  with  $\mathbf{n} = (n_1, n_2, n_3) = (p_1, p_2, p_3) \times (q_1, q_2, q_3)$ ,  $n_i \in \mathbb{Z}$ .

Since the plane-spanning vectors are lattice vectors, the plane is itself periodic and therefore represents a plane lattice. With  $\mathbf{p}$  and  $\mathbf{q}$  as basis vectors of the plane lattice, the plane is periodic along the direction of  $\mathbf{p}$  and  $\mathbf{q}$  with periodicity length  $|\mathbf{p}|$  and  $|\mathbf{q}|$ , respectively. The parallelogram constructed from  $\mathbf{p}$  and  $\mathbf{q}$  represents a unit cell of the plane lattice with a cell area of  $|\mathbf{p} \times \mathbf{q}| = |\mathbf{n}|$ . One can show that there is no smaller unit cell if the integer coefficients  $n_1$ ,  $n_2$ , and  $n_3$  are coprime. Furthermore, there is no shorter non-zero lattice vector perpendicular to the plane than  $\mathbf{n}$  in this case, and hence, the shortest periodicity along the normal direction is  $|\mathbf{n}|$ .

For the computational cube of the Millennium Simulation with side length  $L = 500h^{-1}$  Mpc, the lengths and areas above have to be multiplied by  $L$  and  $L^2$ , respectively. Our choices  $\mathbf{p} = L(3, -1, 0)$  and  $\mathbf{q} = L(1, 3, -1)$  yield a LOS vector  $\mathbf{n} = L(1, 3, 10)$  with  $|\mathbf{n}| = 5.244h^{-1}$  Gpc and a rectangular area of  $1.581h^{-1}$  Gpc  $\times$   $1.658h^{-1}$  Gpc for the lens planes.

## References

- Amendola, L., Kunz, M., & Sapone, D. 2008, *Journal of Cosmology and Astro-Particle Physics*, 4, 13
- Ashcroft, N. W. & Mermin, N. D. 1976, *Solid State Physics* (Philadelphia: Saunders College)
- Bacon, D. J., Taylor, A. N., Brown, M. L., et al. 2005, *MNRAS*, 363, 723
- Bartelmann, M. & Schneider, P. 2001, *Phys. Rep.*, 340, 291
- Benjamin, J., Heymans, C., Semboloni, E., et al. 2007, *MNRAS*, 381, 702
- Blandford, R. & Narayan, R. 1986, *ApJ*, 310, 568
- Bower, R. G., Benson, A. J., Malbon, R., et al. 2006, *MNRAS*, 370, 645
- Colless, M., Dalton, G., Maddox, S., et al. 2003, *VizieR Online Data Catalog*, 7226, 0
- Cooley, J. W. & Tukey, J. W. 1965, *Math. Comput.*, 19, 297
- Cooray, A. & Hu, W. 2002, *ApJ*, 574, 19
- Cooray, A. & Sheth, R. 2002, *Phys. Rep.*, 372, 1
- Crittenden, R. G., Natarajan, P., Pen, U.-L., & Theuns, T. 2002, *ApJ*, 568, 20
- Croton, D. J., Springel, V., White, S. D. M., et al. 2006, *MNRAS*, 365, 11
- De Lucia, G. & Blaizot, J. 2007, *MNRAS*, 375, 2
- Eisenstein, D. J. & Hu, W. 1999, *ApJ*, 511, 5
- Frijo, M. & Johnson, S. G. 2005, *Proc. IEEE*, 93, 216
- Fu, L., Semboloni, E., Hoekstra, H., et al. 2008, *A&A*, 479, 9
- Gavazzi, R., Treu, T., Rhodes, J. D., et al. 2007, *ApJ*, 667, 176
- Gottschalk, S., Lin, M. C., & Manocha, D. 1996, in *SIGGRAPH '96: Proceedings of the 23rd annual conference on Computer graphics and interactive techniques* (New York, NY, USA: ACM Press), 171–180
- Hamana, T. & Mellier, Y. 2001, *MNRAS*, 327, 169
- Hilbert, S., Metcalf, R. B., & White, S. D. M. 2007a, *MNRAS*, 382, 1494
- Hilbert, S., White, S. D. M., Hartlap, J., & Schneider, P. 2007b, *MNRAS*, 382, 121
- Hilbert, S., White, S. D. M., Hartlap, J., & Schneider, P. 2008, *MNRAS*, 386, 1845
- Hockney, R. W. & Eastwood, J. W. 1981, *Computer Simulation Using Particles* (Computer Simulation Using Particles, New York: McGraw-Hill, 1981)
- Hoekstra, H., Mellier, Y., van Waerbeke, L., et al. 2006, *ApJ*, 647, 116
- Jain, B. & Seljak, U. 1997, *ApJ*, 484, 560
- Jain, B., Seljak, U., & White, S. 2000, *ApJ*, 530, 547

- Mandelbaum, R., Seljak, U., Kauffmann, G., Hirata, C. M., & Brinkmann, J. 2006, MNRAS, 368, 715
- Massey, R., Heymans, C., Bergé, J., et al. 2007a, MNRAS, 376, 13
- Massey, R., Rhodes, J., Ellis, R., et al. 2007b, Nature, 445, 286
- Massey, R., Rhodes, J., Leauthaud, A., et al. 2007c, ApJS, 172, 239
- Munshi, D., Valageas, P., van Waerbeke, L., & Heavens, A. 2008, Phys. Rep., 462, 67
- Neto, A. F., Gao, L., Bett, P., et al. 2007, MNRAS, 381, 1450
- Peacock, J. A. & Dodds, S. J. 1996, MNRAS, 280, L19
- Réfrégier, A., Boulade, O., Mellier, Y., et al. 2006, in Presented at the Society of Photo-Optical Instrumentation Engineers (SPIE) Conference, Vol. 6265, Space Telescopes and Instrumentation I: Optical, Infrared, and Millimeter. Edited by Mather, John C.; MacEwen, Howard A.; de Graauw, Mattheus W. M.. Proceedings of the SPIE, Volume 6265, pp. 62651Y (2006).
- Schimd, C., Tereno, I., Uzan, J.-P., et al. 2007, A&A, 463, 405
- Schneider, P. 2006, in Saas-Fee Advanced Course 33: Gravitational Lensing: Strong, Weak and Micro, ed. G. Meylan, P. Jetzer, P. North, P. Schneider, C. S. Kochanek, & J. Wambsganss (Berlin: Springer), 269–451
- Schneider, P., Ehlers, J., & Falco, E. E. 1992, Gravitational Lenses (Berlin Heidelberg New York: Springer-Verlag)
- Schneider, P., van Waerbeke, L., Jain, B., & Kruse, G. 1998, MNRAS, 296, 873
- Schneider, P., van Waerbeke, L., & Mellier, Y. 2002, A&A, 389, 729
- Seitz, S. & Schneider, P. 1996, A&A, 305, 383
- Seitz, S., Schneider, P., & Ehlers, J. 1994, Classical and Quantum Gravity, 11, 2345
- Seljak, U. 2000, MNRAS, 318, 203
- Semboloni, E., Mellier, Y., van Waerbeke, L., et al. 2006, A&A, 452, 51
- Shapiro, C. & Cooray, A. 2006, Journal of Cosmology and Astro-Particle Physics, 3, 7
- Simon, P., Hettterscheidt, M., Schirmer, M., et al. 2007, A&A, 461, 861
- Smith, R. E., Peacock, J. A., Jenkins, A., et al. 2003, MNRAS, 341, 1311
- Spergel, D. N., Verde, L., Peiris, H. V., et al. 2003, ApJS, 148, 175
- Springel, V. 2005, MNRAS, 364, 1105
- Springel, V., White, S. D. M., Jenkins, A., et al. 2005, Nature, 435, 629
- Taylor, A. N., Kitching, T. D., Bacon, D. J., & Heavens, A. F. 2007, MNRAS, 374, 1377
- Tinker, J. L. and Weinberg, D. H. and Zheng, Z. & Zehavi, I. 2007, ApJ, 631, 41
- Vale, C. & White, M. 2003, ApJ, 592, 699
- Wambsganss, J., Bode, P., & Ostriker, J. P. 2004, ApJ, 606, L93
- Wambsganss, J., Cen, R., & Ostriker, J. P. 1998, ApJ, 494, 29